

MorphEUS: Morphable Omnidirectional Unmanned System

Ivan Bao*, José C. Díaz Peón González Pacheco*, Atharva Navsalkar*, Andrew Scheffer*, Sashreek Shankar*, Andrew Zhao*, Hongyu Zhou*, and Vasileios Tzoumas

Abstract—Omnidirectional aerial vehicles (OMAVs) have opened up a wide range of possibilities for inspection, navigation, and manipulation applications using drones. In this paper, we introduce MorphEUS, a morphable co-axial quadrotor that can control position and orientation independently with high efficiency. It uses a paired servo motor mechanism for each rotor arm, capable of pointing the vectored-thrust in any arbitrary direction. As compared to the *state-of-the-art* MAVs, we achieve higher and more uniform force/torque reachability with a smaller footprint and minimum thrust cancellations. The overactuated nature of the system also results in resiliency to rotor or servo-motor failures. The capabilities of this quadrotor are particularly well-suited for contact-based infrastructure inspection and close-proximity imaging of complex geometries. In the accompanying control pipeline, we present theoretical results for full controllability, almost-everywhere exponential stability, and thrust-energy optimality. We evaluate our design and controller on high-fidelity simulations showcasing the trajectory-tracking capabilities of the vehicle during various tasks. Supplementary details and experimental videos are available on the project webpage: <https://iral-morphable.github.io/>.

I. INTRODUCTION

Multicopter aerial vehicles have seen tremendous applications in the real world, including industrial inspection [1], search and rescue [2], and automated crop monitoring [3]. Standard multicopters suffer from limited maneuverability due to their limited controllability: the control of their position and orientation is coupled. This under-actuation heavily compromises their deployment in contact-based inspections, cluttered environments, and sensing and mapping applications. Omnidirectional multicopters (OMAVs) are aerial robots that enhance maneuverability through over-actuation and, in some cases, adaptive rotor configurations. This work introduces a novel MAV (see Fig. 1 for CAD design; Fig. 11 for hardware prototype) capable of pointing the thrust in arbitrary directions. As compared to the *state-of-the-art*, we achieve higher and more uniform force/torque reachability with a smaller footprint and minimum thrust cancellations.

A. Related Work

As multicopter robotic platforms have become more ubiquitous, there has been an increasing demand to extend their maneuverability [4], [5]. Many works in the last decade have

* Authors ordered alphabetically. A.Z. and I.B. contributed to the hardware design. A.S., S.S., and J.D. contributed to the firmware and simulations. H.Z. contributed to the geometric control. A.N. contributed to the control allocation. A.S., S.S., J.D., A.N., and H.Z. contributed to the writing.

This work was conducted at the University of Michigan with the partial support of the Michigan Translational Research and Commercialization (MTRAC) for Advanced Transportation Innovation Hub.

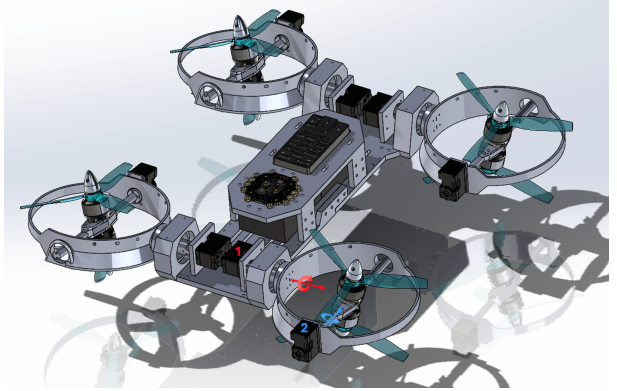


Fig. 1: CAD of the proposed morphable quadrotor actuated with two additional degrees of freedom for each rotor, providing 360° thrust-vectoring capabilities.

focused on developing fully-actuated multicopters that have at least some decoupling of position and orientation. The current literature of fully-actuated multicopters can be divided into two broad classes: 1) *variable-tilt multicopters*, which can actuate the orientation of their rotors during flight, and 2) *fixed-tilt multicopters*, which cannot [6].

Fixed-tilt multicopters like [7]–[9] have rotors mounted at fixed angles relative to the chassis. While this simplifies the mechanical design, it often limits omnidirectional motion, restricts versatility to specific tasks such as constrained navigation, and reduces efficiency due to thrust cancellations. The octorotor configuration in [10] achieves omnidirectional motion using out-of-plane rotor placements enclosed inside a cube. However, it suffers from inefficient force cancellations, no payload capacity, and a large footprint.

Variable-tilt multicopters, such as [11], [12], enable synchronized thrust vectoring for quadrotors, allowing more versatile motion control. However, they face limitations in achieving full force-torque reachability and often impose strict orientation-tracking constraints. The Voliro hexacopter [13], [14], utilizing six independent servos, is one of the most advanced fully-actuated UAVs, offering omnidirectional control. Despite its capabilities, it still faces challenges related to complex mechanics and limited efficiency in certain maneuvers. Similarly, [15] proposes a fully omnidirectional morphable octocopter with rotors that tilt synchronously. This design offers enhanced flexibility but still struggles with thrust inefficiencies and mechanical complexity.

B. Contributions

We present a novel variable-tilt co-axial quadrotor (Figure 1) and a control pipeline (Figure 2) that achieves a

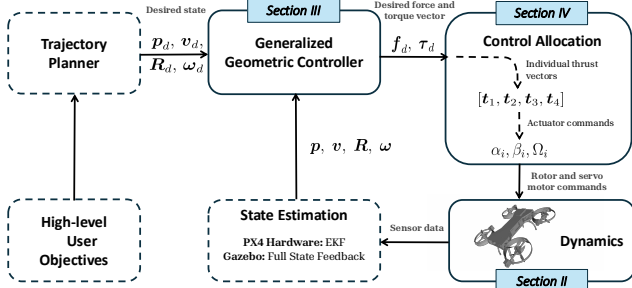


Fig. 2: Autonomous pipeline for the proposed variable-tilt morphable quadrotor.

significantly higher level of maneuverability, dexterity, and efficiency. This system builds on prior work by improving omnidirectional flight capabilities while avoiding inefficient thrust cancellations. To realize this, each of the rotor pairs can be independently oriented using a pair of servo motors (Figure 1). This allows for full 6-DoF control of position and orientation. We prove that the proposed controller is exponentially stable *almost* everywhere and energy-optimal in terms of control allocation. In comparison to existing literature, our contributions are on three broader aspects:

1) *Dexterity and Full Omnidirectionality*: Our quadrotor can achieve all the force-torque realizations (within actuator limits) in all directions. We prove the system is fully controllable and reachable, enabling our drone to traverse complex and constrained geometries. This capability enhances dexterity for inspection and manipulation tasks.

2) *Aggressive Maneuverability*: Unlike [15], our design achieves omnidirectionality with a much smaller footprint, resulting in higher maneuverability. The proposed geometric controller, generalizing [16], has an *almost* 360° region of attraction, enabling the vehicle to achieve exponential stability at almost any configuration in $SO(3)$.

3) *High Efficiency with Resiliency*: Despite being an overactuated system, our control allocation scheme has zero thrust cancellation for translation, compared to [14]. For general force-torque commands, we propose an intuitive and theoretically energy-optimal control allocation strategy. Moreover, our quadrotor design employs co-axial rotors, negating the rotor counter-torques and increasing thrust density. This design is robust for up to three rotor failures due to independent thrust vectoring at each rotor arm.

Figure 2 shows the proposed control pipeline for our quadrotor. We first discuss the dynamics of the quadrotor based on the morphing rotors (actuators) in Section II. There, we expand on the controllability and reachability propositions. Next, in Section III, we present the generalized geometric controller and the results on exponential stability. The low-level control allocation scheme is elaborated in Section IV. Finally, we validate our proposed system using three high-fidelity simulation experiments that demonstrate the 6-DoF tracking capabilities of the quadrotor in Section V.

II. MORPHABLE QUADROTOR DYNAMICS

In this section, we introduce the morphable quadrotor dynamical model. The model consists of the translational

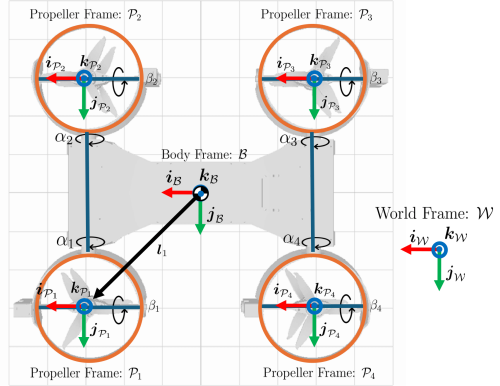


Fig. 3: Schematic of the drone highlighting coordinate frames and servo angles.

dynamics and the rotational dynamics. We use \mathcal{W} to denote the world frame, \mathcal{B} to denote the body-fixed frame, and \mathcal{P} to denote the propeller-fixed frame, shown in Figure 3. We use a $Z - X - Y$ Euler angle sequence for yaw ψ , roll ϕ , and pitch θ to represent the orientation. By design, the *body to propeller* frame transformation is characterized by two angles α and β , as shown in Figure 3. Each of these angles is controlled by a servo motor, providing additional actuator commands alongside the propeller speeds.

A. Translational Dynamics

The translational dynamics of the quadrotor is given by

$$\dot{\mathbf{p}} = \mathbf{v}, \quad m\dot{\mathbf{v}} = mg + \mathbf{R}\mathbf{f}, \quad (1)$$

where $\mathbf{p} \in \mathbb{R}^3$ and $\mathbf{v} \in \mathbb{R}^3$ are position and velocity in the world frame, m is the quadrotor mass, $\mathbf{g} \in \mathbb{R}^3$ is the acceleration due to gravity in the world frame, $\mathbf{R} \in SO(3)$ is the rotation matrix from body to world frame, $\mathbf{f} \in \mathbb{R}^3$ is the body forces generated by propellers in the body frame.

Our design enables the generation of body forces \mathbf{f} in any direction and it can be expressed as

$$\mathbf{f} = \sum_{i=1}^4 (c_t \Omega_i^2) \mathbf{R}_{\mathcal{P}_i/\mathcal{B}}(\alpha_i, \beta_i) \mathbf{k}_{\mathcal{P}_i} = c_t \mathbf{G} \boldsymbol{\Omega}^{\circ 2}, \quad (2)$$

where $\mathbf{R}_{\mathcal{P}_i/\mathcal{B}}(\alpha_i, \beta_i)$ is the body-to-propeller rotation matrix, $\boldsymbol{\Omega} = [\Omega_1, \Omega_2, \Omega_3, \Omega_4]^T$ is the angular rates of propellers, c_t is the thrust coefficient, \circ indicates the Hadamard power, and \mathbf{G} is a suitable matrix that maps angular rates of propellers to body forces.

B. Rotational Dynamics

The rotational dynamics of the quadrotor is given by

$$\dot{\mathbf{R}} = \mathbf{R}[\boldsymbol{\omega}]_\times, \quad \mathcal{J}\dot{\boldsymbol{\omega}} = -\boldsymbol{\omega} \times \mathcal{J}\boldsymbol{\omega} + \boldsymbol{\tau}, \quad (3)$$

where $\boldsymbol{\omega} \in \mathbb{R}^3$ is the angular velocity in the body frame, $[\cdot]_\times : \mathbb{R}^3 \rightarrow \mathbb{R}^{3 \times 3}$ is the skew-symmetric matrix operator, $\mathcal{J} \in \mathbb{R}^{3 \times 3}$ is the inertia matrix in the body frame, and $\boldsymbol{\tau} \in \mathbb{R}^3$ is the torque generated by propellers in the body frame.

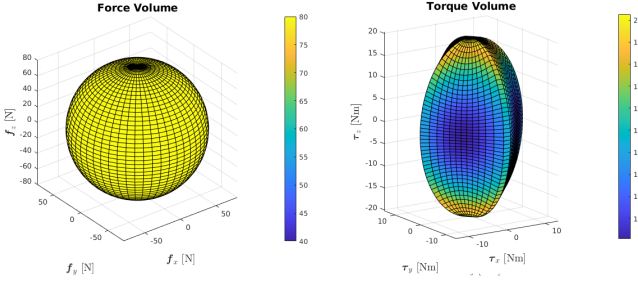


Fig. 4: Force and torque envelopes, assuming that each arm can apply a maximum thrust of 20N. Force envelope assumes desired torque to be zero, and vice versa.

The first term in the angular velocity dynamics is the gyroscopic moment, due to the change in the angular momentum. In the co-axial configuration, we constrain the rotational speed of both the propellers on one arm to be equal. This negates the drag force (angular) of each of the propellers due to equal and opposite spinning co-axial propellers. Since the net angular momentum of the individual pair is zero, it is energy efficient to point the thrust in any direction, using minimal effort from servo motors. The torque τ is only a function of the individual thrust vectors, given by

$$\tau = \sum_{i=1}^4 (c_t \Omega_i^2) \mathbf{l}_i \times \hat{\mathbf{t}}_i, \quad (4)$$

where $\mathbf{l}_i = l_{ix}\mathbf{i}_B + l_{iy}\mathbf{j}_B + l_{iz}\mathbf{k}_B$ is the position vector of the center of the i -th propeller with respect to center of mass (COM) of the quadrotor in the body frame, $\hat{\mathbf{t}}_i \in \mathbb{R}^3$ is the individual thrust direction (unit vector) for each propeller in the body frame. Mathematically, it is expressed by $\hat{\mathbf{t}}_i = \mathbf{R}_{P_i/B}(\alpha_i, \beta_i)\mathbf{k}_{P_i}$. Substituting these relations, the torque exerted by the propellers is given by

$$\tau = \sum_{i=1}^4 (c_t \Omega_i^2) \mathbf{l}_i \times \mathbf{R}_{P_i/B}(\alpha_i, \beta_i) \mathbf{k}_{P_i} = c_t \mathbf{H} \boldsymbol{\Omega}^{\circ 2}, \quad (5)$$

where \mathbf{H} is a suitable matrix that maps angular rates of propellers to body moments.

Now we have a relation that gives both force and torque applied on the quadrotor due to the angular velocities and direction (based on α_i, β_i) of the propellers. Combining the translation and rotational force equations, we have

$$\begin{bmatrix} \mathbf{f} \\ \boldsymbol{\tau} \end{bmatrix} = c_t \begin{bmatrix} \mathbf{G} \\ \mathbf{H} \end{bmatrix} \boldsymbol{\Omega}^{\circ 2} = c_t \mathbf{F}(\alpha_i, \beta_i) \boldsymbol{\Omega}^{\circ 2}. \quad (6)$$

This is a forward dynamics relation that gives the force and torque exerted due to control inputs α_i, β_i and Ω_i .

In Section IV, we present the inverse relation, that is, the control allocation to compute the values of α_i, β_i and Ω_i , for the desired reference force \mathbf{f}_d and torque $\boldsymbol{\tau}_d$. The novel configuration of our quadrotor allows us to command omnidirectional force and torque independently, subject only to the saturation limit of the individual propeller pair.

C. Reachability and Controllability

We discuss that our vehicle is fully controllable and can command omnidirectional force and torque independently. We omit proofs, while highlighting the broad methodology.

Proposition 1 (Reachability). *Given the drone dynamics (1) and (3), force and torque relations (6) and sufficient limits on rotor velocities, all the states $\mathbf{x} = [x, y, z, \dot{x}, \dot{y}, \dot{z}, \phi, \theta, \psi, p, q, r]^T$ (position, linear velocity, orientation, angular velocity) are reachable.*

To prove this, we first consider the concatenation of individual thrust vectors $\mathbf{t} = [t_1 \ t_2 \ t_3 \ t_4]^T \in \mathbb{R}^{12}$ as the virtual control input. Intuitively, we can always find values of actual control inputs α_i, β_i and Ω_i that result in any individual thrust vector \mathbf{t}_i , given that rotor speed Ω_i goes sufficiently high. We can then find that the force-torque vector $[\mathbf{f}, \boldsymbol{\tau}]^T \in \mathbb{R}^6$ can be mapped from the virtual control input $\mathbf{t} \in \mathbb{R}^{12}$ through a linear mapping function $\mathcal{M} : \mathbb{R}^{12} \rightarrow \mathbb{R}^6$. We then show that this has infinite solutions, implying that all forces and torques are possible, and hence all the states are reachable.

Corollary 1 (Controllability). *Since the solution for the linear map \mathcal{M} always exists, we can always find a set of thrust vectors $\vec{\mathbf{t}}_i$, such that a desired force and torque is applied. Mathematically, given vectors \mathbf{f} and $\boldsymbol{\tau}$ there exists $\mathbf{t} = [t_1 \ t_2 \ t_3 \ t_4]^T$ such that $\mathbf{f} = \sum_{i=1}^4 \mathbf{t}_i, \boldsymbol{\tau} = \sum_{i=1}^4 \mathbf{l}_i \times \mathbf{t}_i$. Hence, the system is controllable as all force and torque realizations are possible.*

Accounting for rotor speed limits, we get a range of feasible force and torque values under the individual thrust saturation assumption. Figure 4 shows the possible force and torque vector envelope. The force envelope assumes that the commanded torque is zero and vice versa. We see that the force limits are uniform in all directions, while the torque limits have a minimum-to-maximum limit ratio of roughly 0.5. Particularly, the uniform force reachability across all directions holds a significant advantage over existing state-of-the-art designs such as the VoliroX hexacopter [14], [17], [18], where the force envelope is non-uniform.

Remark 1 (Gimbal Lock). *We emphasize that our quadrotor design has capability to exert force and torque, that is, wrench in any given direction. While this is true in any static state, the controllability is constrained in certain directions, when the angle $\beta = \pm\pi/2$ due to the presence of gimbal lock. This aspect is one of the inherent limitations of the design choice where each arm has a pair of orthogonally placed servo motors (angles α_i and β_i). The quadrotor has the control authority to command the angular velocity Ω_i along \mathbf{k}_{P_i} axis, and angles α_i, β_i along \mathbf{j}_B and \mathbf{i}_{P_i} axes respectively, as seen in Figure 3. When $\beta_i = \pm\pi/2$ i.e., desired force \mathbf{f}_d is along \mathbf{j}_B , we see that axes \mathbf{k}_{P_i} and \mathbf{j}_B align with each other. This is why we lose the control authority along yaw axis \mathbf{k}_B as we cannot command any thrust in $\mathbf{i}_B - \mathbf{j}_B$ plane (only in \mathbf{j}_B direction). We can resolve this issue by introducing a differential thrust controller for yaw angle. During the configuration of the gimbal lock,*

we can appropriately create a differential in thrust vector magnitudes along j_B axis to exert a moment along k_B axis. In practice, we will implement this as a hybrid control strategy when $\beta_i \approx \pm\pi/2$.

III. GEOMETRIC CONTROL

We present a generalized geometric controller for the morphable quadrotor to track desired positions and orientations. The controller aims to calculate the desired force and torque commands in 6-DOF, based on the tracking error in position and orientation. In contrast to the geometric controller of a regular quadrotor [16], the generalized geometric controller of the morphable quadrotor obtains completely decoupled forces and torques that can be calculated independently. This superiority is due to the six-dimensional force and torque reachability presented in Section II.

We first define tracking errors as

$$\begin{aligned} e_p &= p - p_d, \quad e_R = \frac{1}{2} (\mathbf{R}_d^\top \mathbf{R} - \mathbf{R}^\top \mathbf{R}_d)^\vee, \\ e_v &= v - v_d, \quad e_\omega = \omega - \mathbf{R}^\top \mathbf{R}_d \omega_d; \end{aligned} \quad (7)$$

$p_d, v_d, \mathbf{R}_d, \omega_d$ are desired position, velocity, rotation matrix, and angular velocity, and $\vee : SO(3) \rightarrow \mathbb{R}^3$ is the vee map.

The generalized geometric controller calculates the desired force and torque as

$$\begin{aligned} f_d &= -\mathbf{R}^\top (-k_p e_p - k_v e_v - m\mathbf{g} + m\mathbf{a}_d), \\ \tau_d &= -k_R e_R - k_\omega e_\omega + \omega \times \mathcal{J}\omega \\ &\quad - \mathcal{J}\omega \times \mathbf{R}^\top \mathbf{R}_d \omega_d - \mathbf{R}^\top \mathbf{R}_d \dot{\omega}_d, \end{aligned} \quad (8)$$

where $\mathbf{a}_d, \dot{\omega}_d$ are desired acceleration and angular acceleration, k_p, k_v, k_R , and k_ω are positive PD control gains.

Substitute the desired force and moment in eq. (8) to quadrotor dynamics in eq. (1) and eq. (3) gives the corresponding closed loop system dynamics

$$\begin{aligned} \dot{e}_p &= e_v, \\ \dot{e}_v &= \frac{1}{m} (-k_p e_p - k_v e_v), \\ \dot{e}_R &= \frac{1}{2} (\text{tr}(\mathbf{R}^\top \mathbf{R}_d) I - \mathbf{R}^\top \mathbf{R}_d) e_\omega, \\ \mathcal{J}\dot{e}_\omega &= -k_R e_R - k_\omega e_\omega. \end{aligned} \quad (9)$$

Proposition 2 (Exponential Stability Almost Everywhere in $SO(3)$). Consider the controller defined in eq. (8). Suppose that the initial conditions satisfy

$$\begin{aligned} \Psi(\mathbf{R}(0), \mathbf{R}_d(0)) &< 2, \\ \|e_\omega(0)\|^2 &< \frac{2k_R}{\lambda_{\max}(\mathcal{J})} (2 - \Psi(\mathbf{R}(0), \mathbf{R}_d(0))), \end{aligned} \quad (10)$$

where a real-valued error function $\Psi(\cdot, \cdot) : SO(3) \times SO(3) \rightarrow \mathbb{R}$ is defined as $\Psi(\mathbf{R}, \mathbf{R}_d) \triangleq \frac{1}{2} \text{tr}(\mathbf{I} - \mathbf{R}_d^\top \mathbf{R})$. Then, the origin of the closed-loop error dynamics in eq. (9) is exponentially stable.

We obtain exponential stability of the generalized geometric controller for almost every pair of $(\mathbf{R}(0), \mathbf{R}_d(0))$. Specifically, Proposition 2 holds for $\Psi(\mathbf{R}(0), \mathbf{R}_d(0)) < 2$, which indicates the initial attitude error between $\mathbf{R}(0)$ and

$\mathbf{R}_d(0)$ should be less than 180° . In other words, we prove that the closed-loop controller is exponentially stable in almost entire $SO(3)$. This result improves the exponential stability of the geometric controller of a regular quadrotor, which requires initial attitude error between $\mathbf{R}(0)$ and $\mathbf{R}_d(0)$ should be less than 90° [16].

IV. CONTROL ALLOCATION

We describe how we compute the low-level actuator commands α_i, β_i and Ω_i from desired force and torque commands computed from the generalized geometric controller. We present the inverse mapping of the dynamics given in eq. (6) which is an under-determined system due to the over-actuated design of the quadrotor. Since this inverse mapping had infinite solutions, the proposed control allocation is provably energy optimal. Hence, our control allocation is energy optimal resulting in minimum thrust cancellations among the rotor arms. As described further, we provide an intuitive and computationally simple allocation scheme where the thrust vector for each arm consists of independent components for force, roll, pitch, and yaw commands. Note that, since each arm has vectored-thrust in any direction based on α_i and β_i . Using this, we can apply the maximum possible thrust uniformly in all directions, as seen in Figure 4.

The desired force-torque vectors, f_d and τ_d , are computed using the geometric control law (eq. (8)). The low-level commands α_i, β_i , and Ω_i are decoupled with the values for the other arm, hence the resulting thrust vector t_i can be considered an (intermediate) virtual control input. Note that the magnitude $\|t_i\|$ depends on the angular velocity of the propeller Ω_i and direction \hat{t}_i is determined by the values of servo motor angles α_i and β_i . Then we break down the desired force and torque into four components, i.e., net force, roll, pitch and yaw. Each component is equally (in magnitude) distributed to all four arms/propellers such that it does not affect the other component. Mathematically, each thrust vector t_i is a vector sum of its contribution towards net force, roll, pitch and yaw, given by

$$\begin{aligned} t_1 &= \frac{f_d}{4} + \left(\frac{\tau_{x,d}}{4l_y} \right) \mathbf{k}_B + \left(\frac{-\tau_{y,d}}{4l_x} \right) \mathbf{k}_B + \left(\frac{\tau_{z,d}}{4r} \right) \hat{t}_{\psi_1}, \\ t_2 &= \frac{f_d}{4} + \left(\frac{-\tau_{x,d}}{4l_y} \right) \mathbf{k}_B + \left(\frac{-\tau_{y,d}}{4l_x} \right) \mathbf{k}_B + \left(\frac{\tau_{z,d}}{4r} \right) \hat{t}_{\psi_2}, \\ t_3 &= \frac{f_d}{4} + \left(\frac{-\tau_{x,d}}{4l_y} \right) \mathbf{k}_B + \left(\frac{\tau_{y,d}}{4l_x} \right) \mathbf{k}_B + \left(\frac{\tau_{z,d}}{4r} \right) \hat{t}_{\psi_3}, \\ t_4 &= \frac{f_d}{4} + \left(\frac{\tau_{x,d}}{4l_y} \right) \mathbf{k}_B + \left(\frac{\tau_{y,d}}{4l_x} \right) \mathbf{k}_B + \left(\frac{\tau_{z,d}}{4r} \right) \hat{t}_{\psi_4}, \end{aligned} \quad (11)$$

where the values l_x, l_y , and $r = \sqrt{l_x^2 + l_y^2}$ are the half-length, half-breadth and distance from CoM of each propeller. This relation can be represented as a linear map $\mathcal{N} : [f_d, \tau_d]^\top \in \mathbb{R}^6 \rightarrow t \in \mathbb{R}^{12}$. The vectors \hat{t}_{ψ_i} are the unit vectors along the yaw directions, in $i_B - j_B$ plane, as shown in Figure 5. Mathematically, these are given by

$$\begin{aligned} \hat{t}_{\psi_1} &= \begin{bmatrix} -\frac{l_y}{r} & \frac{l_x}{r} & 0 \end{bmatrix}^\top, \quad \hat{t}_{\psi_2} = \begin{bmatrix} \frac{l_y}{r} & \frac{l_x}{r} & 0 \end{bmatrix}^\top, \\ \hat{t}_{\psi_3} &= \begin{bmatrix} \frac{l_y}{r} & -\frac{l_x}{r} & 0 \end{bmatrix}^\top, \quad \hat{t}_{\psi_4} = \begin{bmatrix} -\frac{l_y}{r} & -\frac{l_x}{r} & 0 \end{bmatrix}^\top. \end{aligned} \quad (12)$$

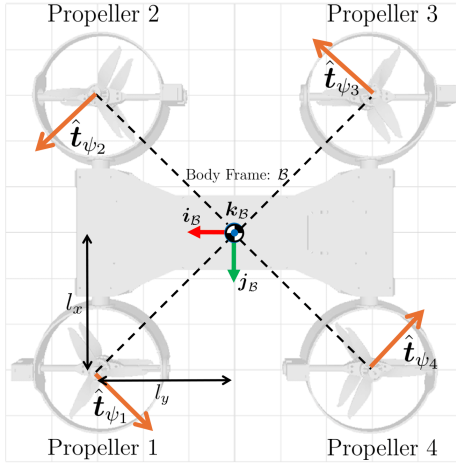


Fig. 5: Unit vectors in $i_B - j_B$ for yaw control.

Finally, from the value of each thrust vector t_i , we can now find the values of α_i , β_i and Ω_i . Based on the rotation matrix $R_{P_i/B}(\alpha_i, \beta_i) = R_{j_{P_i}}(\alpha_i)R_{i_{P_i}}(\beta_i)$, we have t_i as

$$t_i = c_t \Omega_i^2 [\sin \alpha_i \cos \beta_i \quad -\sin \beta_i \quad \cos \alpha_i \cos \beta_i]^\top. \quad (13)$$

We can obtain multiple solutions (α_i, β_i values) for this equation. Due to angle wrapping for inverse trigonometric functions, by design, we define:

$$\Omega_i = \sqrt{\|t_i\|/c_t}, \quad \beta_i = -\sin^{-1}(\hat{t}_{i,y}), \quad (14)$$

$$\alpha_i = \begin{cases} \pi - \sin^{-1}\left(\frac{\hat{t}_{i,x}}{\cos \beta_i}\right) \in (\pi/2, \pi) \\ \quad \text{if } t_{i,z} < 0 \text{ and } t_{i,x} \geq 0, \\ -\pi - \sin^{-1}\left(\frac{\hat{t}_{i,x}}{\cos \beta_i}\right) \in (-\pi, -\pi/2) \\ \quad \text{if } t_{i,z} < 0 \text{ and } t_{i,x} < 0, \\ \sin^{-1}\left(\frac{\hat{t}_{i,x}}{\cos \beta_i}\right) \in [-\pi/2, \pi/2] \\ \quad \text{otherwise.} \end{cases} \quad (15)$$

We can show that this control allocation design is optimal in the sense of sum-of-squares of the energy consumption (where energy is assumed to be proportional to Ω_i^2).

Proposition 3 (Energy-efficient Control Allocation). *The control allocation given by eq. (11) to find thrusts t_1, t_2, t_3, t_4 , for given f_d and τ_d , is the optimal solution with respect to the cost function $E(t_i) = \frac{1}{2} \sum_{i=1}^4 \|t_i\|^2$.*

This can be shown by solving the optimization for minimizing the above cost function subject to the constraints $f = \sum_{i=1}^4 t_i$, $\tau = \sum_{i=1}^4 l_i \times t_i$. Lagrangian multiplier method can be used to show that the proposed inverse mapping (eq. (11)) is the solution. Alternatively, we can show that the linear (inverse) map $\mathcal{N} : [f_d, \tau_d]^\top \in \mathbb{R}^6 \rightarrow t \in \mathbb{R}^{12}$ is pseudo-inverse of forward dynamics mapping $\mathcal{M} : t \in \mathbb{R}^{12} \rightarrow [f, \tau]^\top \in \mathbb{R}^6$, i.e., $N = M^\dagger = M^T (MM^T)^{-1}$. We know that this gives a minimum-norm squared solution for the under-determined system with infinite solutions.

V. SIMULATION EXPERIMENTS

In this section, we present the experimental results demonstrating the proposed quadrotor design and the corresponding controller's performance in inspection-inspired applications.

A. Continuous Contact-based Inspection

For the first experiment, we highlight a potential application of our drone design for contact-based inspection tasks. Figure 6 demonstrates our vehicle's ability to orient an attached tool in arbitrary directions with precision. In this experiment, we affix a black tool to the vehicle and trace a controlled trajectory along the surface of a water tower. As the vehicle ascends, it dynamically pitches to maintain proper tool alignment. Upon reaching the top, it transitions into a descent by yawing about its body z-axis while continuously keeping the tool in contact with the surface. This controlled interaction illustrates the system's dexterity and ability to maintain precise tool orientation, expanding the range of tasks achievable with aerial robots beyond what is possible with conventional multirotors.

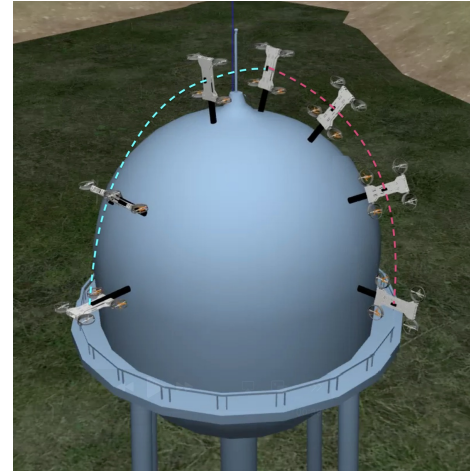


Fig. 6: Our quadrotor following a continuous-contact trajectory on a simulated water tower. During ascent (blue) and descent (red), it dynamically orients its fixed tool (black rod) to be normal to the structure.

Figure 7 and Figure 8 demonstrate our controller's effectiveness in tracking position and orientation during the maneuver. As shown in Figure 7, the quadrotor's ground truth position precisely tracks the commanded position of the trajectory. Additionally, Figure 8 indicates that throughout the entire maneuver, the orientation error never surpasses 0.0035 radians.

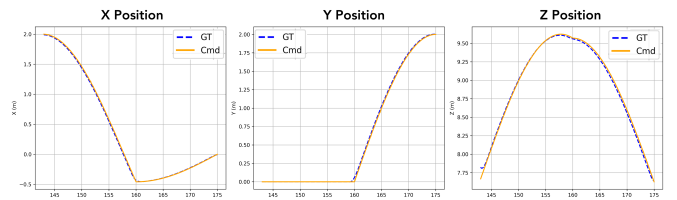


Fig. 7: Translational trajectories for commanded water tower trajectory. The vehicle position (blue dashed) closely follows the commanded position (orange solid).

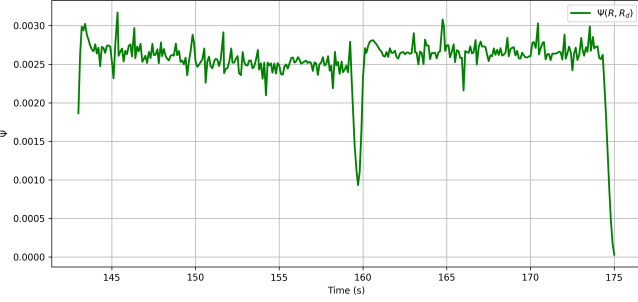


Fig. 8: Orientation error, $\Psi(R, R_d)$, for commanded water tower trajectory.

B. Flying in Constrained Spaces

Next, we demonstrate our quadrotor’s ability to follow 6-DoF trajectories in constrained spaces. Figure 9 highlights how the enhanced maneuverability of our quadrotor enables it to navigate successfully through a narrow pipe structure. The vertical section of the pipe imposes strict spatial constraints, limiting the feasible orientations that the quadrotor can achieve without collision. Our system’s adaptability enables it to traverse these tight spaces.

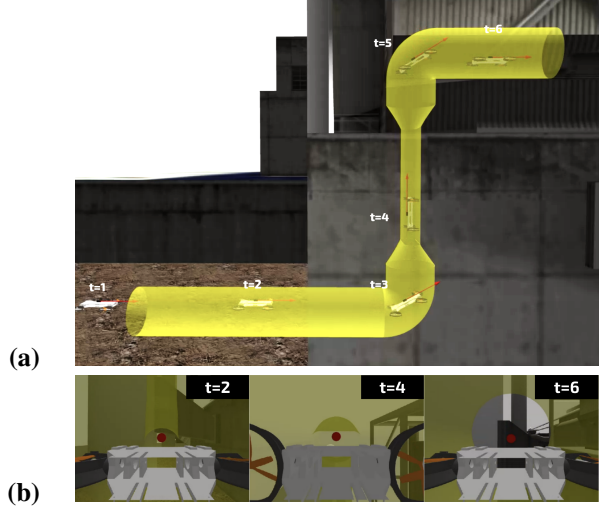


Fig. 9: (a) The morphable quadrotor tracking a trajectory inside a constrained conduit and (b) first-person-view inspection images from a body-mounted camera.

C. Continuous Visual Inspection

Finally, to showcase the system’s 6-DoF trajectory-following capabilities, we design an experiment in which the quadcopter follows a corkscrew trajectory while continuously keeping a fixed camera aimed at a central object. Unlike current multirotors, which are limited in their ability to maintain precise viewpoint control during complex maneuvers, our system leverages its extended maneuverability to smoothly follow the trajectory while ensuring the target remains consistently framed. Figure 10 presents both a third-person perspective of the trajectory and a corresponding first-person view from the body-fixed camera.

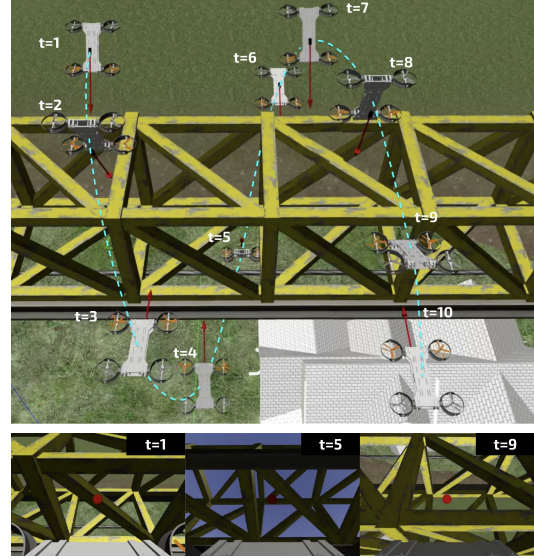


Fig. 10: (a) The morphable quadrotor tracking a corkscrew trajectory (dotted blue line) around an object for 10 distinct timesteps and (b) the corresponding first-person-view inspection images from a body-mounted camera. The red vector represents the optical axis of the camera.

VI. CONCLUSION

We presented a novel variable-tilt quadrotor and accompanying control pipeline that achieves high levels of maneuverability and hand-like dexterity. By independently actuating each rotor’s orientation, our vehicle enables optimally energy-efficient 6-DoF control of position and orientation, enabling the vehicle to stably achieve almost any configuration in $SO(3)$. We demonstrate applications of this quadrotor in simulations: (i) maintaining continuous contact with surfaces during flight, (ii) flying in constrained spaces, and (iii) continuous vision-based inspection.

In future work, we plan to apply these algorithms in real-world experiments. Progress has already been made in this direction, including: (i) extending the algorithms herein to the PX4 [19] software-in-the-loop flight stack, (ii) fabricating the drone (Figure 11), and (iii) conducting preliminary flight tests. For more information, please visit our project website.¹

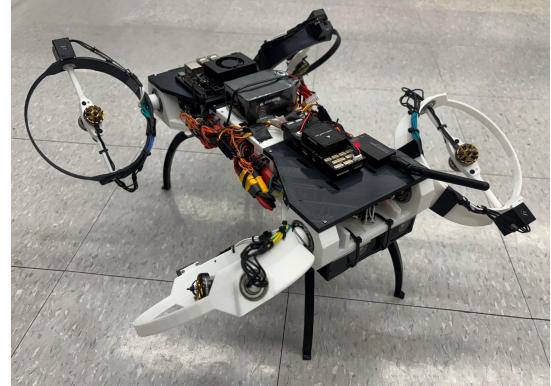


Fig. 11: Prototype of the morphable quadrotor.

¹<https://iral-morphable.github.io/>

REFERENCES

- [1] D. Seneviratne, L. Ciani, M. Catelani, D. Galar *et al.*, “Smart maintenance and inspection of linear assets: An industry 4.0 approach,” *Acta Imeko*, vol. 7, pp. 50–56, 2018.
- [2] S. Waharte and N. Trigoni, “Supporting search and rescue operations with uavs,” in *2010 international conference on emerging security technologies*. IEEE, 2010, pp. 142–147.
- [3] J. Cuaran and J. Leon, “Crop monitoring using unmanned aerial vehicles: A review,” *Agricultural Reviews*, vol. 42, no. 2, pp. 121–132, 2021.
- [4] K. Bodie, M. Brunner, M. Pantic, S. Walser, P. Pfändler, U. Angst, R. Siegwart, and J. Nieto, “Active interaction force control for contact-based inspection with a fully actuated aerial vehicle,” *IEEE Transactions on Robotics*, vol. 37, no. 3, pp. 709–722, 2021.
- [5] A. Ollero, M. Tognon, A. Suarez, D. Lee, and A. Franchi, “Past, present, and future of aerial robotic manipulators,” *IEEE Transactions on Robotics*, vol. 38, no. 1, pp. 626–645, 2022.
- [6] R. Rashad, J. Goerres, R. Aarts, J. B. Engelen, and S. Stramigioli, “Fully actuated multirotor uavs: A literature review,” *IEEE Robotics & Automation Magazine*, vol. 27, no. 3, pp. 97–107, 2020.
- [7] G. Jiang and R. Voyles, “Hexrotor uav platform enabling dexterous interaction with structures—flight test,” in *Proc. 2013 IEEE Int. Symp. Safety, Security, and Rescue Robotics (SSRR)*, 2013.
- [8] S. Rajappa, M. Ryll, H. H. Bühlhoff, and A. Franchi, “Modeling, control and design optimization for a fully-actuated hexarotor aerial vehicle with tilted propellers,” in *Proc. 2015 IEEE Int. Conf. Robotics and Automation (ICRA)*, 2015, pp. 4006–4013.
- [9] Y. Lei, Y. Ji, C. Wang, Y. Bai, and Z. Xu, “Aerodynamic design on the non-planar rotor system of a multi-rotor flying robot (mfr),” in *Proc. 2017 IEEE 3rd Int. Symp. Robotics and Manufacturing Automation (ROMA)*, 2017.
- [10] D. Brescianini and R. D’Andrea, “Design, modeling and control of an omni-directional aerial vehicle,” in *2016 IEEE international conference on robotics and automation (ICRA)*. IEEE, 2016, pp. 3261–3266.
- [11] M. Ryll, H. H. Bühlhoff, and P. R. Giordano, “A novel overactuated quadrotor unmanned aerial vehicle: Modeling, control, and experimental validation,” *IEEE Trans. Control Syst. Technol.*, vol. 23, no. 2, pp. 540–556, Mar. 2015.
- [12] P. Segui-Gasco, Y. Al-Rihani, H.-S. Shin, and A. Savvaris, “A novel actuation concept for a multi rotor uav,” *J. Intell. Robot. Syst.*, vol. 74, no. 1–2, pp. 173–191, Apr. 2014.
- [13] M. Kamel, S. Verling, O. Elkhathib, C. Sprecher, P. Wulkop, Z. Taylor, R. Siegwart, and I. Gilitschenski, “The voliro omniorientational hexacopter: An agile and maneuverable tilttable-rotor aerial vehicle,” *IEEE Robotics & Automation Magazine*, vol. 25, no. 4, pp. 34–44, 2018.
- [14] K. Bodie, Z. Taylor, M. Kamel, and R. Siegwart, “Towards efficient full pose omnidirectionality with overactuated mavs,” in *Proceedings of the 2018 International Symposium on Experimental Robotics*. Springer, 2020, pp. 85–95.
- [15] Y. Aboudorra, C. Gabellieri, R. Brantjes, Q. Sablé, and A. Franchi, “Modelling, analysis, and control of omnimorph: an omnidirectional morphing multi-rotor uav,” *Journal of Intelligent & Robotic Systems*, vol. 110, no. 1, p. 21, 2024.
- [16] T. Lee, M. Leok, and N. H. McClamroch, “Geometric tracking control of a quadrotor uav on $se(3)$,” in *49th IEEE conference on decision and control (CDC)*. IEEE, 2010, pp. 5420–5425.
- [17] M. Allenspach, K. Bodie, M. Brunner, L. Rinsoz, Z. Taylor, M. Kamel, R. Siegwart, and J. Nieto, “Design and optimal control of a tiltrotor micro-aerial vehicle for efficient omnidirectional flight,” *The International Journal of Robotics Research*, vol. 39, no. 10-11, pp. 1305–1325, 2020.
- [18] K. Bodie, M. Brunner, and M. Allenspach, *Omnidirectional Tilt-Rotor Flying Robots for Aerial Physical Interaction: Modelling, Control, Design and Experiments*. Springer Nature, 2023, vol. 157.
- [19] L. Meier, D. Honegger, and M. Pollefeys, “Px4: A node-based multithreaded open source robotics framework for deeply embedded platforms,” in *2015 IEEE International Conference on Robotics and Automation (ICRA)*, 2015, pp. 6235–6240.